Contents lists available at ScienceDirect

# Electrochimica Acta

journal homepage: www.journals.elsevier.com/electrochimica-acta





# Electrolyte ohmic heating during electrodeposition: The role of coupled kinetic-transport phenomena that lead to morphological and microstructural changes

Pınar Eribol <sup>a,1</sup>, Sarathy K. Gopalakrishnan <sup>b,c,1</sup>, S.V. Diwakar <sup>d</sup>, Abdelkrim Talbi <sup>a</sup>, Ranga Narayanan<sup>b</sup>, Farzam Zoueshtiagh<sup>a,\*</sup>, Kirk J. Ziegler<sup>b,\*</sup>

- a Univ. Lille, CNRS, Centrale Lille, Junia, Université de Polytechnique Hauts-de-France, UMR 8520 IEMN Institut d'Electronique de Microélectronique et de Nanotechnologie, F-59000 Lille, France
- b Department of Chemical Engineering, University of Florida, Gainesville, FL 32611, USA
- <sup>c</sup> Department of Materials Science and Engineering, University of Florida, Gainesville, FL 32611, USA
- <sup>d</sup> Engineering Mechanics Unit, JNCASR, Jakkur, Bangalore, 560064, India

## ARTICLE INFO

#### Keywords: Electrodeposition Copper sulfate Copper Morphology Concentration Electrochemistry Instability Convection

## ABSTRACT

Understanding the morphological changes to the electrodes during electrochemical processes is important to many fields. These morphological changes often lead to dendrite formation and significant heat generation that can be detrimental to the process, especially the performance and lifetime of batteries. In situ infrared thermometry and microscopy are used to study the evolution of temperature profiles during the microscale electrodeposition of copper from copper sulfate. Under certain conditions, the growth front of the deposit receded and the fastest growing dendrites would suddenly stop growing. Analysis of physicochemical, temperature, and current changes show that many dynamic phenomena are correlated and associated with localized pH changes that change the chemistry of electrodeposition and potential drops occurring across the electrodes that alter the transport around dendrites.

### 1. Introduction

Electrodeposition is a fundamental electrochemical process studied by many over the past several decades [1-7]. The reduction of metal ions is a dynamic phenomenon that is a combination of ion transport and a charge transfer reaction mechanism giving rise to a morphological evolution at the cathode. Understanding the morphology of the deposits and the coupled kinetic-transport mechanisms influencing the growth is imperative to various applications, including the fabrication of complex structures in 3D metal additive printing [8], electrodeposition of thin films/interconnects in microelectronic manufacturing [9-11], and in prolonging the performance and lifetime of batteries [12].

The growth of electrodeposition patterns at the cathode occurs due to random disturbances at the electrode surface. These disturbances occur from perturbations or inhomogeneities that lead to instability phenomenon [13-16], resulting in non-uniform (or wavy) deposition [17]. The inhomogeneities can be any physical difference, such as surface roughness and different crystallographic orientation, or any localized effects, such as local variations in concentration, transport, surface states, and even a slight vibration in the laboratory. Any disturbance at the cathode or anode alters the potential and concentration gradients locally and either enhances or diminishes the reactions at the surface. Due to these changes, any perturbation at the anode will be suppressed, while a perturbation at the cathode will be self-reinforcing and grow, resulting in a positive feedback mechanism [18].

The positive feedback mechanism encourages well-defined periodic patterns to grow at the cathode surface. The pattern that grows is selected by the competition between kinetics, transport, and interfacial surface energy, which promote the growth of the instability towards a single dominant wavelength. The dominant wavelength (periodicity) of structures formed due to the instability can be theoretically predicted using linear stability analysis [19–25]. The linear growth rate  $(\sigma)$  vs. the inverse square of every possible disturbance wavelength (whose reciprocal is expressed as wavenumber squared,  $k^2$ ) obtained for copper electrodeposition is broad near the maximum, which suggests that there

<sup>1</sup> These authors contributed equally.

<sup>\*</sup> Correspondence to: Institut d'Electronique de Microélectronique et de Nanotechnologie (IEMN) CNRS, 8520 Avenue Poincaré-CS 60069 59652 Villeneuve d'Ascq, France.

Correspondence to: 1006 Center Drive, Gainesville, FL 32611, USA. E-mail addresses: farzam.zoueshtiagh@univ-lille.fr (F. Zoueshtiagh), kziegler@che.ufl.edu (K.J. Ziegler).

are many competing wavelengths growing with comparable growth rates. Therefore, longer timescales are required for the system to select the dominant wavelength. However, longer timescales allow non-linear interactions that lead to the formation of dendritic branches and obscure the underlying instability pattern. We have recently shown that the occurrence of dendritic branches can be delayed by encouraging the growth to happen in shorter timescales, i.e., by using narrow electrode spacing and promoting the growth to occur in a quasi 1-D manner [18]. Delaying the onset of dendritic branches were shown to result in experimental wavelengths within 5% and largely within 1% of the theoretical wavelength predicted by the instability model [18].

While the growth of dendritic branches can be delayed, they cannot be completely avoided in electrodeposition [18]. The morphology of the electrodeposition patterns are dependent on the input parameters (such as voltage, spacing, and electrolyte concentration). The various deposition morphologies observed in copper electrodeposition have been classified as either [26]:

- Compact: A non-structured, dense morphology with an absence of ramification, and typically has slow growth rates advancing towards the anode;
- Homogeneous: Deposits exhibiting regularly spaced tree-like structures with their advancing growth front parallel to the cathode:
- Open: Morphologies characterized by self-similar structures with high ramification. The growth rate of the branches is nonuniform, and the growth front of the branches are not necessarily parallel to the cathode; and
- Dendritic: Deposits with straight structures and considerable ramification. Unlike homogeneous deposits, dendritic deposits have irregular advancing growth rates, with a few structures growing faster than the rest.

Although copper-copper sulfate electrodeposition is one of the simplest electrochemical systems taught in basic electrochemistry courses, the process still involves several coupled phenomena. The copper at the anode is dissolved into cupric ions, which are subsequently reduced to elemental copper metal at the cathode. The initial concentration alters the bulk pH of the electrolyte, which determines the specific chemical reactions that occur at the surface. However, these surface reactions involve phase changes and generate local changes in the concentration and pH of the electrolyte [27]. The anode and cathode are also altered during dissolution and deposition, which can lead to local ohmic heat generation around the electrodes [28]. These temperature changes subsequently alter the chemical reactions at the electrode surface. The concentration and thermal gradients lead to convection within the cell [29]. If these coupled phenomena result in significant changes at the electrode, the deposition morphology may be dynamic during the process [26].

Branched finger-like, dendritic structures are beneficial to sensors [30], 3D neuromorphic engineering [31], and space-based applications [32,33] but they are detrimental in lithium-ion battery applications. Recent battery fire/explosion incidents revealed that the growth of lithium dendrites lead to an internal short circuit [34]. For example, several Samsung Galaxy Note 7 tablets that caught fire in 2016 were attributed to these factors, leading to a thermal runaway cascade within the battery [35].

Because of the importance in safety, performance, and lifetime, understanding the temperature profile and heat generation in electrochemical systems has become increasingly important. For example, exothermic reactions yield finger-pattern formations and hot spots in the exothermic front [36]. These hotspots increased convection and locally enhanced the reaction and consequently the temperature, demonstrating the coupling of the exothermic reactions with diffusion and convective processes. Barkey et al. [37] noticed that non-uniform ohmic heating at the deposits decreases both the density and the

viscosity of the solution near the interface. Schröter et al. [38] used IR thermometry to visualize the temperature field. They showed that the deposits act like an effective heat sink, and the thermal gradients that occur at the electrodes provide the weak driving force to the concentration gradient-driven convection rolls. Simulations by Barvinschi [39] were found to qualitatively match the experimental findings of Schröter et al. [38].

In this work, non-invasive infrared (IR) thermometry [40] is employed to investigate heat formation and dissipation during electrodeposition. IR thermometry images provide 2D spatial evolution of the temperature profile of the electrodeposition process with high resolution without interfering with the system. This is an advantage over thermocouples since they only measure the temperature at a fixed point and the flow dynamics can be altered. Even though IR thermometry has been used to understand the temperature effects in reactive systems before [41,42], to the best of our knowledge, Schröter et al. [38] is the only study that employed IR thermometry in thin-layer electrodeposition of Zn. While Schröter et al. [38] showed that electrolyte heating is prevalent in thin-layer deposition, the results were limited to a single operating condition. In this work, we studied the effect of the initial electrolyte concentration on the temporal evolution of the temperature profile within the electrochemical cell during electrodeposition. Our results show that the temperature distribution within the cell depends on various coupled factors, including the initial bulk concentration, the pH of the solution, and dynamic transitions in the morphology and microstructure of the growing deposits. Furthermore, the evolution of temperature profiles helped understand how various phenomena were correlated and associated with morphological and microstructural changes to the cathode during electrodeposition.

# 2. Experimental methods

A schematic view of the experimental setup is shown in Fig. 1. The electrochemical cells were assembled on a 0.7 mm thick polystyrene holder of sterile cleanroom ISO-6 quality (VWR International®). Polystyrene was chosen because it is transparent to 3–5  $\mu m$  infrared (IR) wavelengths corresponding to the sensitivity range of the camera (FLIR A8581). Two 35  $\mu m$  thick copper foils with an adhesive backing (McMaster-Carr®) were placed parallel and facing each other (at a spacing distance of L=6 mm) on the polystyrene holder. All foil surfaces but the two sides facing each other were inactivated by covering them with polyimide tapes (McMaster-Carr®) to insulate them from the electrolyte. Therefore, only the 35  $\mu m$  side of the copper foil was an active electrode during experiments. In all experiments, the dimensions of the electrochemical cell were set as 10 mm  $\times$  6 mm, where 6 mm is the spacing between the electrodes (anode to cathode distance) and 10 mm is the length of the electrodes.

The electrochemical cell was constructed by sandwiching 1 mL of electrolyte solution between the polystyrene holder and a 7.6 mm thick PMMA plate (PLEXIGLAS®). The PMMA plate was used as a back shielding cover to avoid any IR interference from the atmosphere. IR spectra were observed from the polystyrene window from below (see Fig. 1). This configuration made the heat variation visible during electrodeposition. Although the electrolyte is water based and absorbs IR light in the 3–5  $\mu m$  range of the camera, the attenuation is not enough to prevent a signal from the thin electrochemical cell from reaching the camera. Calculations show an IR attenuation of 50% at 3  $\mu m$  and 99% at 20  $\mu m$  thick water film, assuming the average absorption coefficient of mid-IR wavelengths in water is around 100 mm $^{-1}$  [43].

The electrolyte solution was prepared using anhydrous copper sulfate crystals (CuSO $_4$ ; Carl Roth $^{\circledR}$  and purity  $\geq 99\%$ ) dissolved in deionized water at concentrations of 5, 50, 200, and 400 mM. The pH of the copper sulfate electrolyte at different concentrations was measured using a Fisher Scientific AET15 pH meter. Before taking measurements, the pH meter was calibrated using 4, 7, and 10 pH buffer solutions.

P. Eribol et al. Electrochimica Acta 462 (2023) 142616

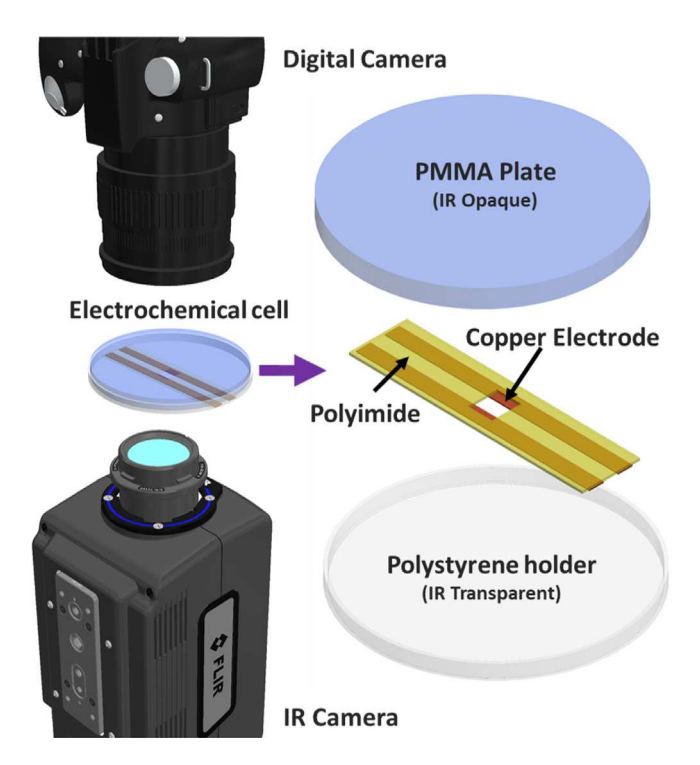


**Fig. 1.** Schematic of the experimental setup. Electrochemical cell constructed on an IR transparent polystyrene holder using adhesive copper tape and covered with an IR opaque PMMA plate. Polyimide tape was used to inactivate portions of the surface. The cell is placed between the digital and IR cameras to capture the growth and temperature profiles.

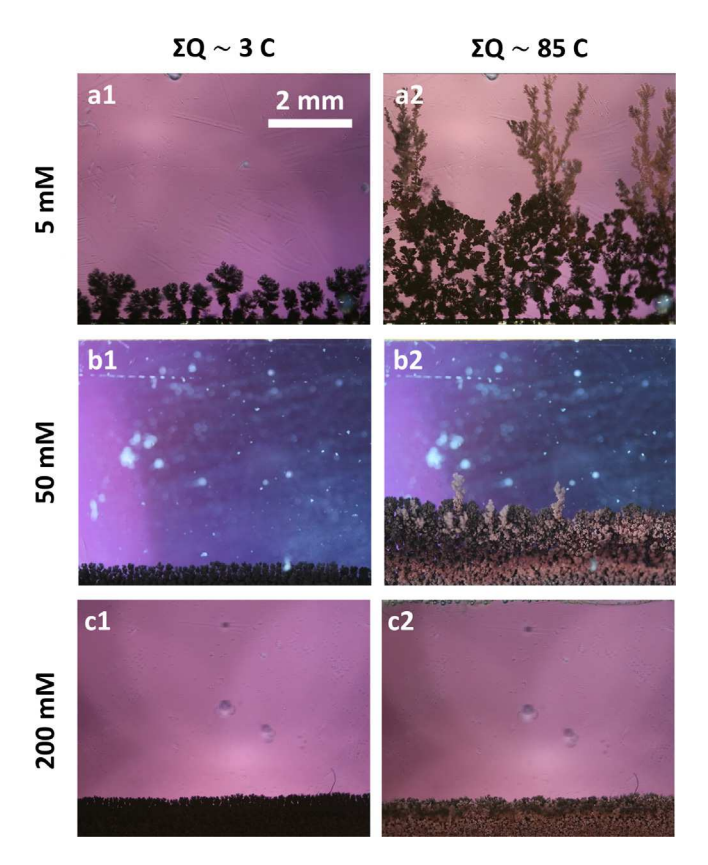


Fig. 2. The morphology of the deposited copper at early (total charge of  $\approx 3$  C) and late (total charge of  $\approx 85$  C) stage deposition for  $\text{CuSO}_4$  concentrations of 5, 50, and 200 mM.

A two-electrode configuration was used throughout this study and the electrochemical cell was operated at constant voltage using a Keysight B2901BL precision source/measurement unit. An input voltage of 7 V (accuracy:  $\pm 1~\mu V$ ) was applied, and the output current was recorded with an accuracy of  $\pm 1~pA$ . The total charge required to grow the deposition patterns at any given time was calculated by integrating the current (*I*) with respect to time (*t*) from chronoamperometric data. The Pourbaix diagram of CuSO<sub>4</sub> at different concentrations (20 °C, 1 atm) were plotted using the Geochemist's workbench software.

The growth patterns that form at the cathode during electrodeposition were recorded in real-time (30 fps; 3840 × 2160 resolution) from the top of the electrochemical cell using a NIKON D850 Digital camera with a 3x objective lens (Laowa 25 mm F2.8 Ultra Macro 2.5-5×). A ring light source was used to illuminate the cell from the top. A high-definition mid-wavelength infrared camera (FLIR A8581, Teledyne FLIR, In-Sb sensor; spectral range of 3-5 μm; temperature sensitivity of 30 mK; 12  $\mu m$  pixel size; 1280  $\times$  1024 resolution) with a 1x close-up/microscope lens was located at a distance of 30 cm to the cell and used to record real-time thermographic videos at 30 fps from the bottom of the electrochemical cell (see Fig. 1). The digital and IR cameras were spatially locked and synchronized to record the entire field of view of the electrochemical cell simultaneously. The analysis of the thermographic videos was performed using FLIR ResearchIR (Teledyne FLIR) software. Background correction was applied by subtracting the first frame to obtain the absolute temperature change in the system and eliminate the Narcissus effect. The Narcissus effect is an undesirable effect common in infrared cameras caused by the sensor detecting itself due to reflection from the substrate surface. An emissivity value of 0.96 was assumed for water in the experiments [44].

The growth front (or height) of dendritic structures is difficult to characterize, especially when some of the structures grow much faster and can be sparsely dispersed across the cathode. In this work, dendritic structures appeared to be responsible for a lot of the observed behavior. To capture their potential influence, it was necessary to define their height beyond a baseline value. The baseline was chosen to be the average growth for all deposits. The average growth front for the dendrites was then taken to be the third quartile of the height distribution (bottom 75% of all heights). If a uniform film is deposited, the average growth front of dendrites would then be indistinguishable from the average. The deposit growth front (height) was measured from the digital camera images using ImageJ software [45]. A trace of the growth front was first drawn, defining the ROI (region of interest). Subsequently, the Y coordinates (Y = 0 at the cathode and Y = 6 mm at the anode) of the envelope were extracted using the getSelectionCoordinates macro [46]. Here each *Y* coordinate corresponds to a pixel at the growth front along the width of the image. The average growth front of the dendrites was then determined by calculating the third quartile of the Y coordinates. The height calculated this way better represented the influence of the dendrites on the measured temperature profiles than a mean of all Y coordinates.

The local pH changes within the electrochemical cell were studied using fluorescence microscopy. A pH-sensitive fluorescence dye (1 mM LysoSensor Green DND-189, Thermo Fisher Scientific) was added to copper sulfate solution to yield a concentration of 9.9  $\mu$ M. The electrodeposition was performed under an Olympus BX51 fluorescence microscope with a U-MNIBA3 filter cube (with 470 – 495 nm excitation filter and 510 – 550 nm emission filter) and the cell was observed under a 1.25× objective lens. The fluorescence intensity changes due to local pH variation in the cell during electrodeposition were captured every 2 s using a NIKON D850 digital camera (F1.8; ISO 800; exposure 0.5 s).

# 3. Results

Electrodeposition of copper was conducted in a two-electrode micro-electrochemical cell. Depending on the electrolyte concentration used, a variety of deposition morphologies were observed and

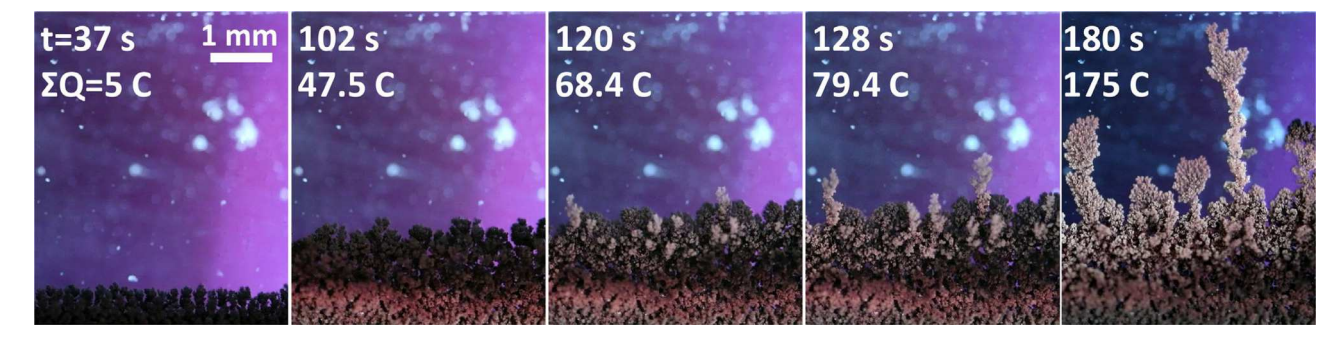


Fig. 3. The time evolution of electrodeposition for an electrolyte concentration of 50 mM. Note that the microstructure of the deposits transition from a fine and dark reddish appearance at the early stages to a coarser, bright, and metallic appearance at the later stages.

classified using the nomenclature established by Sagués et al. [26]. Fig. 2 shows the different deposit morphologies observed at the initial and later stages of electrodeposition for different electrolyte concentrations. Initial deposits in experiments at low electrolyte concentrations (5 and 50 mM) displayed homogeneous morphology (see a1, b1 of Fig. 2) where the deposited patterns had similar growth rates and were regularly and closely spaced. As electrodeposition progressed, the morphology changes. Later deposits seen in 5 mM concentration has ramifications and the interspace between the structures are wide as opposed to the initial morphology, indicating a transition to open structures. The same is true for the morphology seen in 50 mM concentration, except the structures have fewer ramifications, indicating a change to dendritic morphology. At high concentrations (200 mM), the initial deposits showed compact morphology (see c1 of Fig. 2) with a slow advancing growth rate. No changes to morphology were observed at this concentration.

In all cases, the initial deposits are small grains that have a dark reddish appearance. These color differences can be observed as distinct layers in the deposit, as shown in a2 and b2 of Fig. 2 for 5 and 50 mM concentration experiments, respectively. These distinct layers can be seen more clearly as the electrodeposition progresses in Fig. 3. Dark red deposits exist at the earliest stage. The next stage (around  $t=102~\rm s$ ) shows that the deposits continue to be dark red in nature but those deposits closest to the cathode appear to change in color. Once dendrites start to form (after  $t=120~\rm s$ ), the deposits were coarser, bright, and metallic in appearance. As electrodeposition progresses further, the dark reddish deposits seem to disappear, leaving only bright, metallic structures.

In addition to the distinct layers and colors observed, Fig. 4 shows that the growth front can shrink during electrodeposition. This receding growth front is much more clearly observed in Vid. 1. This volume change of the interface indicates that microstructural changes must also be occurring during this transition.

In order to study these changes and their potential role on the instabilities that form, infrared thermography data was also collected. The temperature changes in the electrolyte solution during electrodeposition were captured as a time series of heatmaps using the IR camera. Fig. 5a shows the temporal evolution of the copper morphology and the corresponding thermal map within the electrochemical channel for 5 mM electrolyte concentration. A small but uniform increase in temperature is observed throughout the cell during the initial stages. Once dendritic formations are observed, localized heating can be observed, as seen at t = 165 s. These dendritic structures continue to be localized sources of heat throughout deposition. Fig. 5b show the temperature profile across the electrochemical channel along the line AC (A: anode and C: cathode; L = 6 mm). On application of voltage, the electrolyte temperature increases slightly. In the initial stages ( $t \le 30$  s), the height of the deposits is small and the temperature profile is relatively flat. As electrodeposition progresses, the temperature increases and the profile has a temperature maximum that lies approximately at the average growth front of the dendritic structures. It is important to note that this

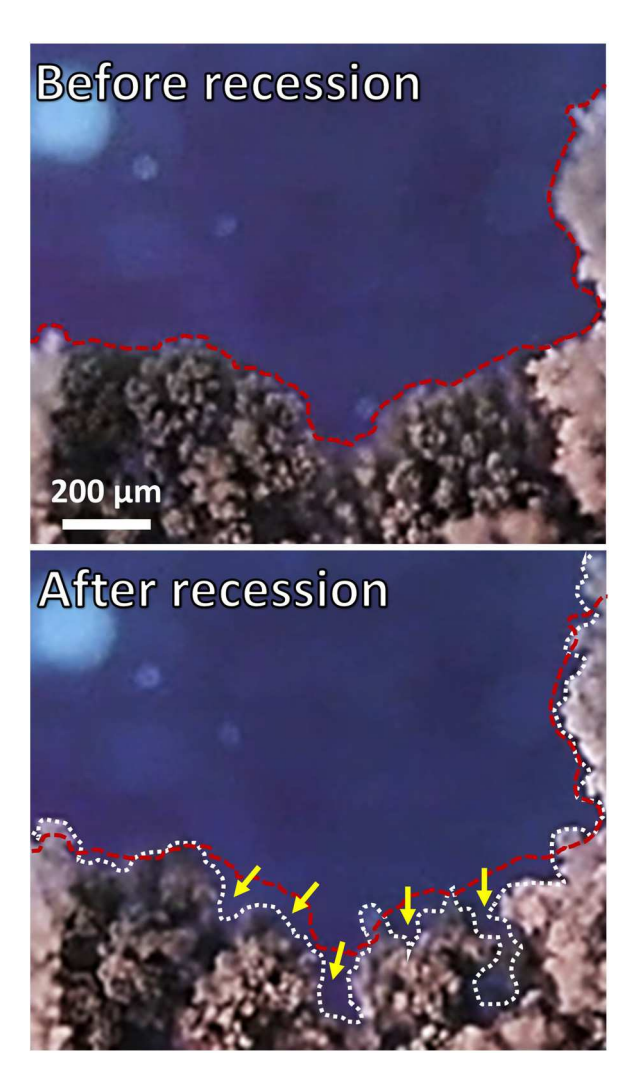


Fig. 4. Swift recession of the growth front observed during electrodeposition for an electrolyte concentration of  $50\,$  mM.

is the moving front of the cathode as deposition occurs. Fig. 5c shows the average temporal temperature changes at specific fixed points in the electrochemical cell measured along AC. The temperature rise in the middle of the cell ( $y = \frac{1}{4}L$ ,  $y = \frac{1}{2}L$ , and  $y = \frac{3}{4}L$ ) is relatively consistent and steady in the initial stages. In the range between 100 and 150 s, deviations start to form that appear to correspond to the time at which dendrites start to form.

Similar temperature changes are observed in experiments with 50 mM electrolyte concentration. As shown in Fig. 6a, it is observed

P. Eribol et al. Electrochimica Acta 462 (2023) 142616

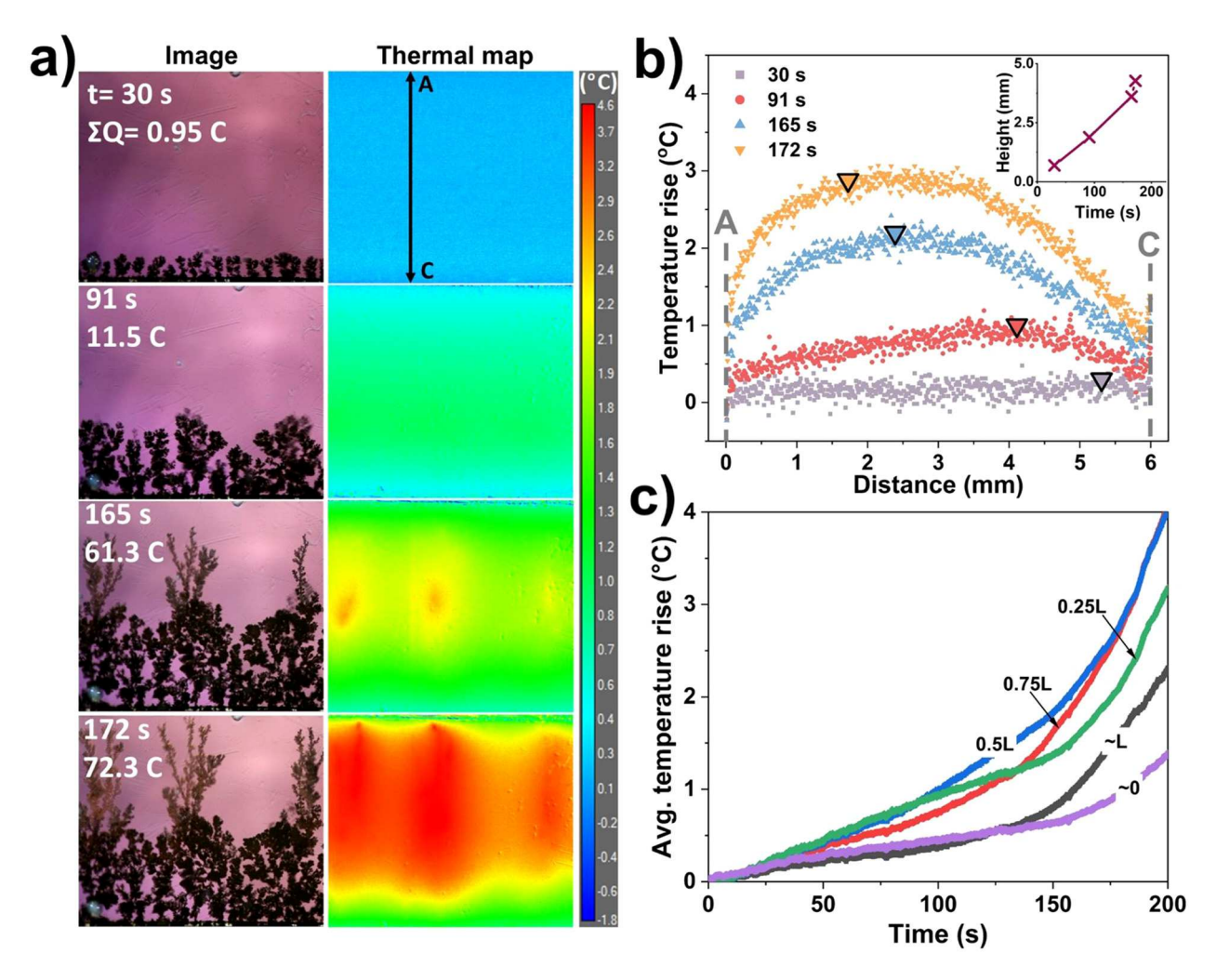


Fig. 5. (a) The evolution of electrodeposited morphology and the corresponding thermal map at an electrolyte concentration of 5 mM for L=6 mm. (b) The temperature profile measured across the (A)node to (C)athode within the electrochemical cell (inset figure: deposit height as a function of time). The inverted triangles represent the average growth front of dendrites past the baseline growth front. (c) Temporal changes of the average temperature at specific points in the electrochemical cell.

again that the temperature increases slowly and uniformly until dendrites start to form. At that point, significant localized heating can be observed with the temperature rising locally by 6 °C. Fig. 6b shows that the temperature profile is concave parabolic, where the temperature maximum lies approximately at the dendritic growth front. As electrodeposition progresses, the shape of the temperature profile across the channel takes an asymmetric shape (first distinguishable at t = 87 s and later in Fig. 6b) while the overall temperature of the electrolyte keeps increasing. Unlike the anode, the profile near the cathode becomes linear until the temperature maximum represented by the growth front of the dendrites (edge of cathode). The linear part of the temperature profile grows with time, and it clearly coincides with the average dendritic growth front. Fig. 6c shows the initial average temperature rise in the middle of the cell  $(y = \frac{1}{4}L, y = \frac{1}{2}L)$ , and  $y = \frac{3}{4}L$ ) is consistent and steady for approximately 100 s. After this point, the deviations that form in the temperature changes are more clearly associated with the time at which dendrites start to form.

For experiments conducted at high electrolyte concentrations of 200 and 400 mM, slightly different temperature profiles are attained from those at low concentration experiments. Fig. 7a shows the temporal evolution of the copper morphology and the corresponding thermal map within the electrochemical channel at 200 mM concentration. Unlike the low concentration experiments, Fig. 7b shows that both anode—and cathode—electrolyte interfaces heat up and reach a higher temperature than the bulk electrolyte at the beginning of the experiment (t=

7 s), creating a convex parabolic profile. The shape of the temperature profile remains similar as the overall temperature of the electrolyte increases. At t=21 s, the temperature profile becomes nearly uniform inside the bulk electrolyte and it becomes a concave parabolic profile similar to those observed at lower concentrations. At longer times, the anode continues to heat up and the temperature profile becomes linear between the two electrodes. The temporal changes in Fig. 7c show different behavior as well. A rapid rise in temperature is seen until approximately t=21 s and then a sudden decrease in temperature is observed. After a short cooling period, the electrolyte closest to the anode continues to heat up. Similar behavior is seen for experiments at 400 mM concentration, as shown in Fig. S1. At this concentration, the temperature changes are not as high but the transition to a linear profile between electrodes is faster.

Another phenomena observed was the cessation of growth of the fastest-growing branch. Fig. 8 shows a dendrite that is growing from the cathode. Localized heating around the dendrite becomes apparent after  $t=48\,$  s. As electrodeposition progresses, the growth of this structure slows considerably. While the growth of the dendrite has slowed, notice that the region to the right of the dendrite starts growing at a much faster rate. The deposition in this region also has a different color than the earlier growth. Eventually, the deposits in this region start to appear brighter as well.

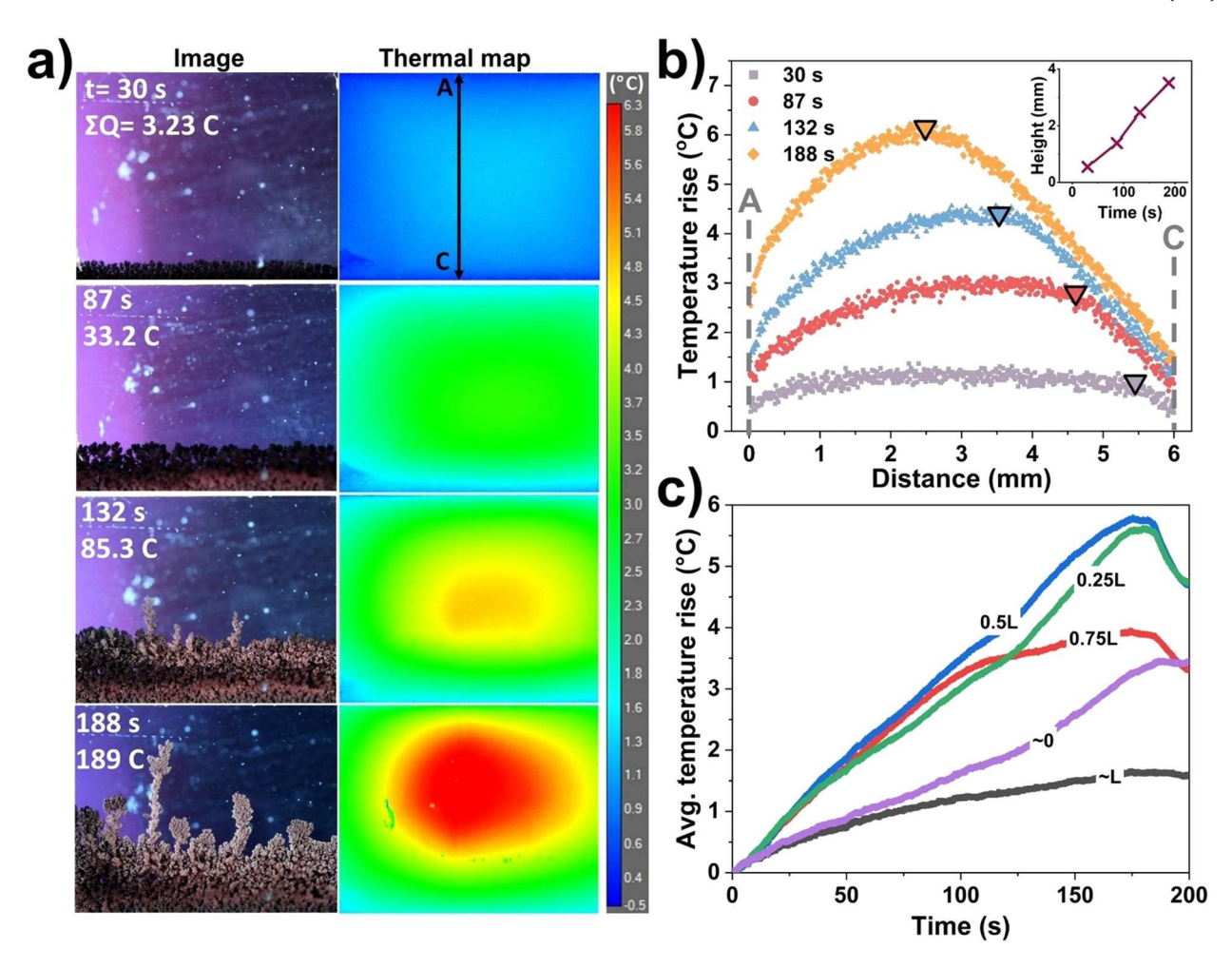


Fig. 6. (a) The evolution of electrodeposited morphology and the corresponding thermal map at an electrolyte concentration of 50 mM for L = 6 mm. (b) The temperature profile measured across the (A)node to (C)athode within the electrochemical cell (inset figure: deposit height as a function of time). The inverted triangles represent the average growth front of dendrites past the baseline growth front. (c) Temporal changes of the average temperature at specific points in the electrochemical cell.

# 4. Discussion

The data clearly demonstrate that changes in morphology, microstructure, and temperature occur throughout electrodeposition. Fig. 3 shows color changes during deposition, which indicate that the chemistry is changing as time progresses. The receding growth front in Fig. 4 and Vid. 1 indicates that the microstructure of the deposit changes with time too. These dynamic microstructural and morphological transitions are collectively known as the Hecker effect and have been observed in prior studies [27,38,47–49]. X-ray powder diffraction results from other work on deposits grown in 50 mM CuSO<sub>4</sub> solution have found that the initial deposits consist of  $\sim$ 40% Cu<sub>2</sub>O as opposed to later deposits with  $\sim$ 20% Cu<sub>2</sub>O [26]. Although copper metal is the anticipated deposition at the cathode, the pH of the solution affects the chemistry [29]. From the half-reactions at the anode,

$$Cu(s) \to Cu^{2+}(aq) + 2e^{-} \tag{1}$$

$$2Cu(s) + H_2O \rightarrow Cu_2O(s) + 2e^- + 2H^+$$
 (2)

and the cathode,

$$Cu^{2+}(aq) + 2e^{-} \rightarrow Cu(s)$$
(3)

$$2Cu^{2+}(aq) + 2e^{-} + 2OH^{-} \rightarrow Cu_2O(s) + H_2O$$
 (4)

the formation/deposition of  ${\rm Cu_2O}$  is pH-dependent, as shown in the Pourbaix diagrams generated for different concentrations of  ${\rm CuSO_4}$  in

Fig. 9a. From the Pourbaix diagram in Fig. 9a,  $Cu_2O$  formation at the anode and deposition at the cathode becomes more likely when the local pH  $\gtrsim 3$ . Since the pH of our electrolyte solutions are between 4.1 and 5.3,  $Cu_2O$  deposition is likely. However, significant  $Cu_2O$  deposition consumes  $OH^-$  groups near the electrode through Eq. (4), causing the local pH to be more acidic and enabling the deposition of copper. In addition,  $Cu_2O$  deposits can transform to copper through another electrochemical reaction when the pH  $\lesssim 3$ :

$$Cu_2O(s) + 2H^+ + 2e^- \rightarrow 2Cu(s) + H_2O$$
 (5)

Therefore, the formation of both Cu and  $\rm Cu_2O$  can occur during electrodeposition. The microstructural change observed in our experiments could be due to local pH changes that occur as electrodeposition progresses, which triggers the transition of  $\rm Cu_2O$  in the deposits to copper metal [29,49]. Since the volume of  $\rm Cu_2O$  is larger than copper, the transition causes the growth front to contract.

To further investigate the role that pH has during electrodeposition, a fluorescent, pH-sensitive dye was added to the electrolyte. Vid. 2 shows local pH changes within the electrochemical cell during electrodeposition in 200 mM  ${\rm CuSO_4}$  solution. It is apparent that a pH gradient exists in the cell at the start of deposition with the pH near the anode being more acidic. As deposition progresses, however, a moving front of acid approaches the cathode. The point when the acid front reaches the cathode coincides with the microstructural transition.

The time at which the microstructural transition occurs varies with the initial concentration of the electrolyte. The microstructural transition occurs earlier in higher concentrations of electrolyte. For 400 mM P. Eribol et al. Electrochimica Acta 462 (2023) 142616

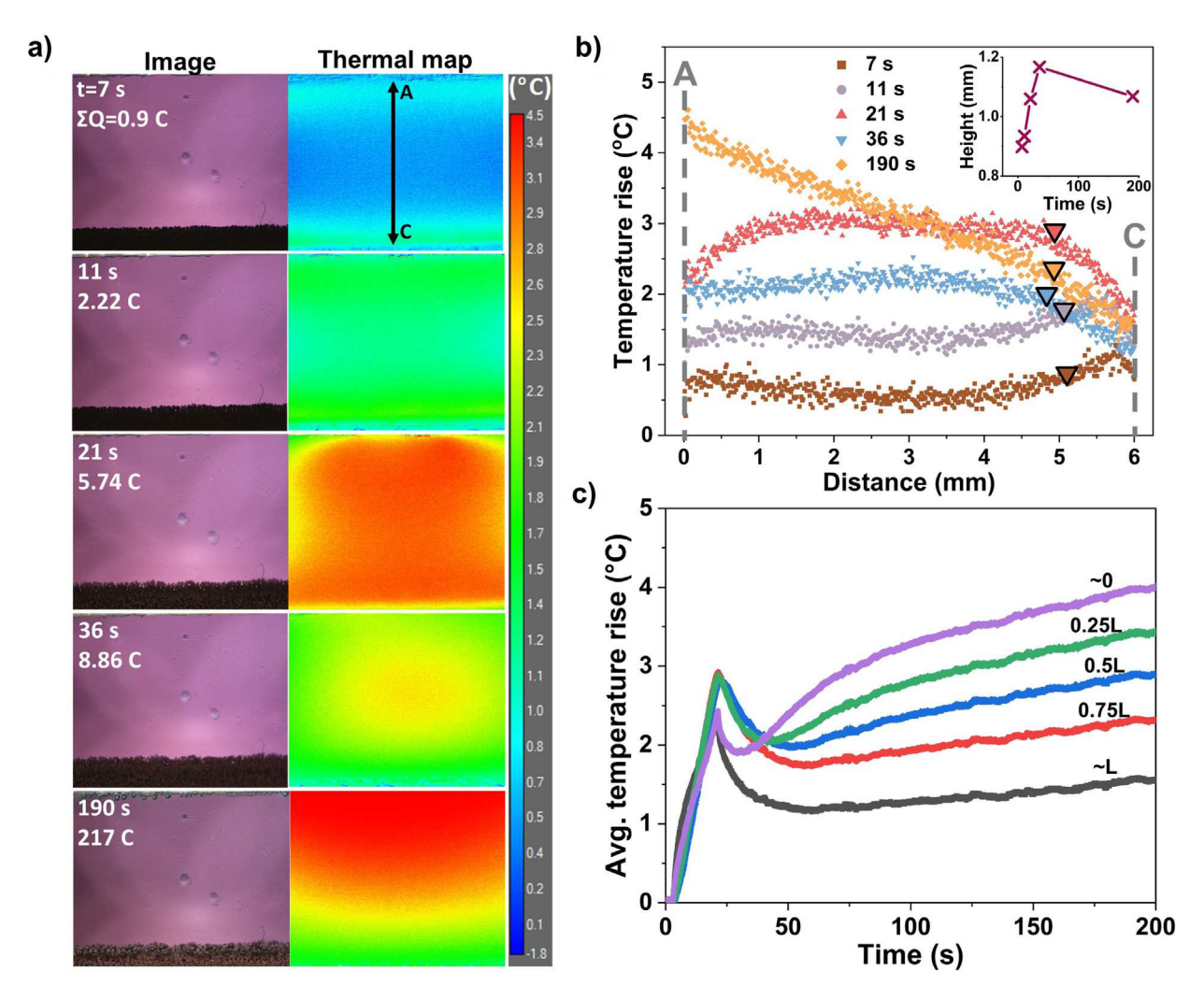


Fig. 7. (a) The evolution of electrodeposited morphology and the corresponding thermal map at an electrolyte concentration of 200 mM for L = 6 mm. (b) The temperature profile measured across the (A)node to (C)athode within the electrochemical cell (inset figure: deposit height as a function of time). The inverted triangles represent the average growth front of dendrites past the baseline growth front. (c) Temporal changes of the average temperature at specific points in the electrochemical cell.

concentration, the transition occurs at an average of 4 s from the application of voltage. In contrast, it can take up to 140–155 s to see the transition in 5 mM concentration. These time scales correlate very well with the bulk pH of the electrolyte, as shown in Fig. 9b, as well as the pH change needed to reach the Cu domain of the Pourbaix diagram. Therefore, the initial concentration will determine the extent of Cu<sub>2</sub>O deposition and the transition pH in the Pourbaix diagram will determine how much acid ( $\Delta$ pH) needs to build up near the electrode to initiate the transformation of Cu<sub>2</sub>O.

Another phenomena observed was that the microstructural transition only occurred on later deposits in 5 mM electrolyte concentration. In other words, the transformation and recession of prior  $\mathrm{Cu_2O}$  layers did not occur. In contrast, the microstructural transition/recession was seen on the entire deposit irrespective of when they were formed at higher concentrations. Once again, the lack of complete transformation in the 5 mM electrolyte concentration could be due to an insufficient amount of  $\mathrm{H^+}$  ions to trigger the transition in the deposits either by a lack of generation or transport to the interface. Due to the lack of  $\mathrm{H^+}$ , the recession behavior was not witnessed in 5 mM concentration experiments, as the older deposits are not undergoing the microstructural change. Since no recession is observed, the conversion of  $\mathrm{Cu_2O}$  to  $\mathrm{Cu}$  is not occurring and explains why the early deposits remain dark in color throughout the experiment (contrary to 50, 200, and 400 mM concentrations).

The results demonstrate that there are several complex processes occurring during electrodeposition. In addition, it appears that many of the observed phenomena (morphology, temperature, and current changes) may be correlated, indicating that many of the processes are coupled. For example, heat will be generated in the electrochemical cell due to high resistance and the amount generated will depend on the total current delivered. Therefore, the temperature is expected to rise inside the electrochemical cell. However, anything that causes a change in the resistance (or current) of the electrochemical cell, such as the composition of the cathode/anode, can cause further heat and temperature changes.

To help identify these potential correlations, Gantt charts were used to identify the times at which specific events or phenomena were observed. Fig. 10 shows the Gantt chart for 200 mM electrolyte concentration (other concentrations are shown in Fig. S2–S4). The chart clearly indicates that several of the observed phenomena are correlated to specific times associated with the transformed microstructure (B1) and the establishment of steady state current (B2). Importantly, it can be observed that morphological, temperature, and current changes are occurring simultaneously after completion of the microstructural transition. The correlations are best observed at 200 mM concentrations since the microstructural transition does not occur too early or too late and the time of the transition is relatively narrow.

As the microstructural transition is dependent on the pH, the build up of acid near the cathode will depend on the reaction rate (function of

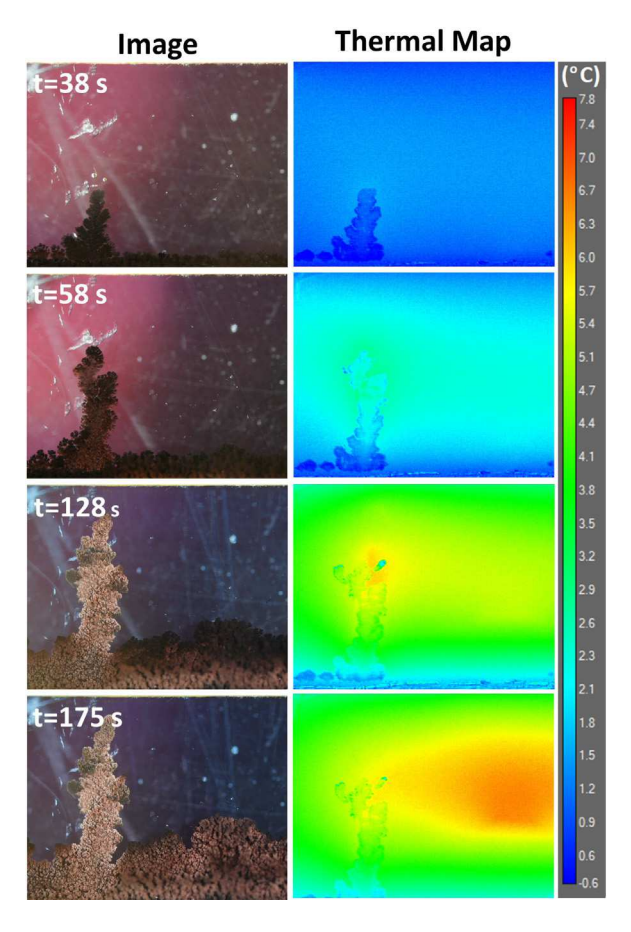


**Fig. 8.** The evolution of deposited morphology and the corresponding thermal map of the fastest growing branch at an electrolyte concentration of 50 mM. Note that dendrite growth slows but deposits to the right start growing faster.

electrical current, pH, and concentration) as well as the mass transport of H<sup>+</sup> (function of electrical current, temperature, and fluid convection associated with thermal differences in the electrolyte). Therefore, different phenomena are anticipated if either the kinetic rates or transport rates are altered. Fig. 11 shows the total charge passed through the electrochemical cell as a function of time. The inset shows a typical current–time plot. After an initial spike and plateau in current, the current suddenly drops and then starts to rise steadily again to another plateau. The charge data shows this transition period is more pronounced for the higher electrolyte concentrations and is not easily observed for the lower concentrations. The transition also occurs much later in the experiment for lower electrolyte concentrations. This is analogous to the observations of the microstructural transition, which occurred earlier for higher concentrations.

The total charge presented in Fig. 11 is proportional to the amount of copper deposited. Therefore, the data also demonstrate that changes to chemistry are occurring throughout the experiment. Others have shown that changes to film growth rate are correlated to the kinetics and transport at the interface [50–53]. Distinct regions can be observed that depend on the limitations of various reactions or the transport of species involved in those reactions. The linear regions of Fig. 11 indicate that different phenomena occur at distinct points during electrodeposition. The kinetics and transport that dictate deposition are similar at different stages of the process and across different concentrations since they have similar slopes of ~2. It appears that the factors driving electrodeposition at early stages return after this transitory period in the current since the slope before and after are nearly identical, which is best exemplified at 200 mM concentration. This again supports that this transitory period in current is associated

with the new chemistry associated with the microstructural transition from  $\text{Cu}_2\text{O}$  to Cu.

For electrodeposition to occur, a steady supply of  $Cu^{2+}$  and  $e^-$  need to reach the interface of the cathode. However, the localized temperature changes observed in the thermography can also cause changes to the chemistry (see Pourbaix diagram Fig. S5) and transport of species to the interface. The nonlinear shape of the temperature profiles observed in Figs. 5–7 indicate that convective heat transfer is occurring at the cathode interface. As the deposition progresses and the growth front becomes a significant portion of the electrochemical cell, the temperature profiles become linear near the cathode. The linear portion indicates that conductive heat transfer is the only means of transporting heat in this region. These linear regions are most easily recognized in the lowest electrolyte concentrations. This linearity would be expected since the solid cathode would be the main path for heat transport through this region.

The temperature profiles are also able to capture the receding growth front. The inset of Fig. 7b shows the average growth front as a function of time. The receding of the deposit height is completed after approximately 50 s. The average temperature rises at various points in the cell shown in Fig. 7c also have a transition of behavior at approximately 50 s where all points in the cell begin to steadily rise in temperature after the transition. In addition, the start of the cooling period observed is clearly associated with the microstructural transition and its end is associated with reaching a steady current (see Fig. 10).

Deposition at higher electrolyte concentrations (200 and 400 mM) clearly have an initial spike in temperature near the electrodeelectrolyte interface (e.g., Fig. 7c). The total charge transferred, and, thus, the heat generated during the first 5 s is proportional to the initial electrolyte concentration (see Fig. S6). The compact growth of deposits at higher concentrations maintains electric field lines that are more uniform, which should reduce convection. On the other hand, a smoother surface reduces drag, allowing convection currents to be maintained. In the initial deposition, the field lines appear to be dominating the behavior. This can be observed by the changes in shape of the temperature profiles at the different concentrations (part b in Figs. 5-7), indicating lower convection. The lack of convective heat transfer and significantly higher heat generation in the early stages causes the temperature to rise quickly at the electrode-electrolyte interfaces at high electrolyte concentration. As convection rolls start to develop, heat is dissipated from the interface through convection that yields flatter profiles near the cathode. As the microstructural transition occurs, the current falls and the amount of heat generated falls, giving a brief cooling period.

It is clear from Figs. 5a and 8 that the tips of the dendrites become the point at which significant heat generation occurs. It can also be observed that the highest temperatures in the profiles are observed at the growth front (e.g., Fig. 6b). The local heating at the growth interface could result from multiple effects. The tip of the deposits at the growth front is thin and may not dissipate heat as fast as the bulk deposits, leading to a local temperature rise at the copper-electrolyte interface. At the same time, the high electric field density around the sharp curvature of the thin tips will speed the formation of deposits on the dendrites. This fast deposition is likely to result in more defects in the copper crystal deposits. The high defect density will increase the electrical resistance through the dendrites. As the resistance increases, the amount of heat generated will increase locally. Similarly, the local spike in temperature observed near the anode-electrolyte interface at high electrolyte concentrations (e.g., Fig. 7a and b) could be due to structural changes in the electrode. As electrodeposition progresses, Cu is being removed from the anode. At high current, significant pitting of the electrode can be observed. This porosity in the electrode would increase the resistance through the anode and cause localized heating [54-56].

These changes to resistance at the electrode, especially when dendrites are formed, can eventually cause potential drops across the

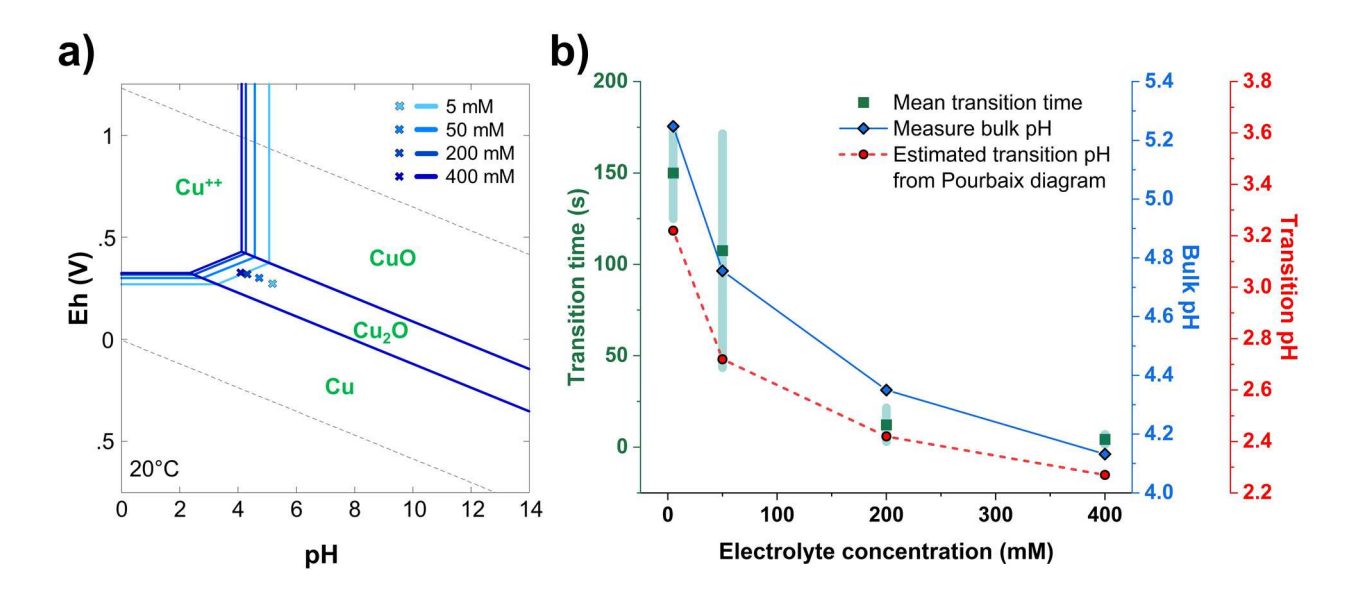


Fig. 9. Effect of electrolyte pH on the copper electrochemical system. (a) Pourbaix diagram of  $CuSO_4$  at different concentrations (20 °C, 1 atm). The potential on the y-axis is with respect to the standard reduction potential. The crosses in the plot show the standard cell potential at different initial concentrations of  $CuSO_4$  at their experimentally measured pH. (b) Correlation of the microstructural transition time with the initial bulk pH of the  $CuSO_4$  electrolyte solution and the local pH required to initiate the microstructural transition (i.e., distance to  $Cu-Cu_2O$  line) as a function of electrolyte concentration. The vertical bars represent the time period associated with the microstructural transition.

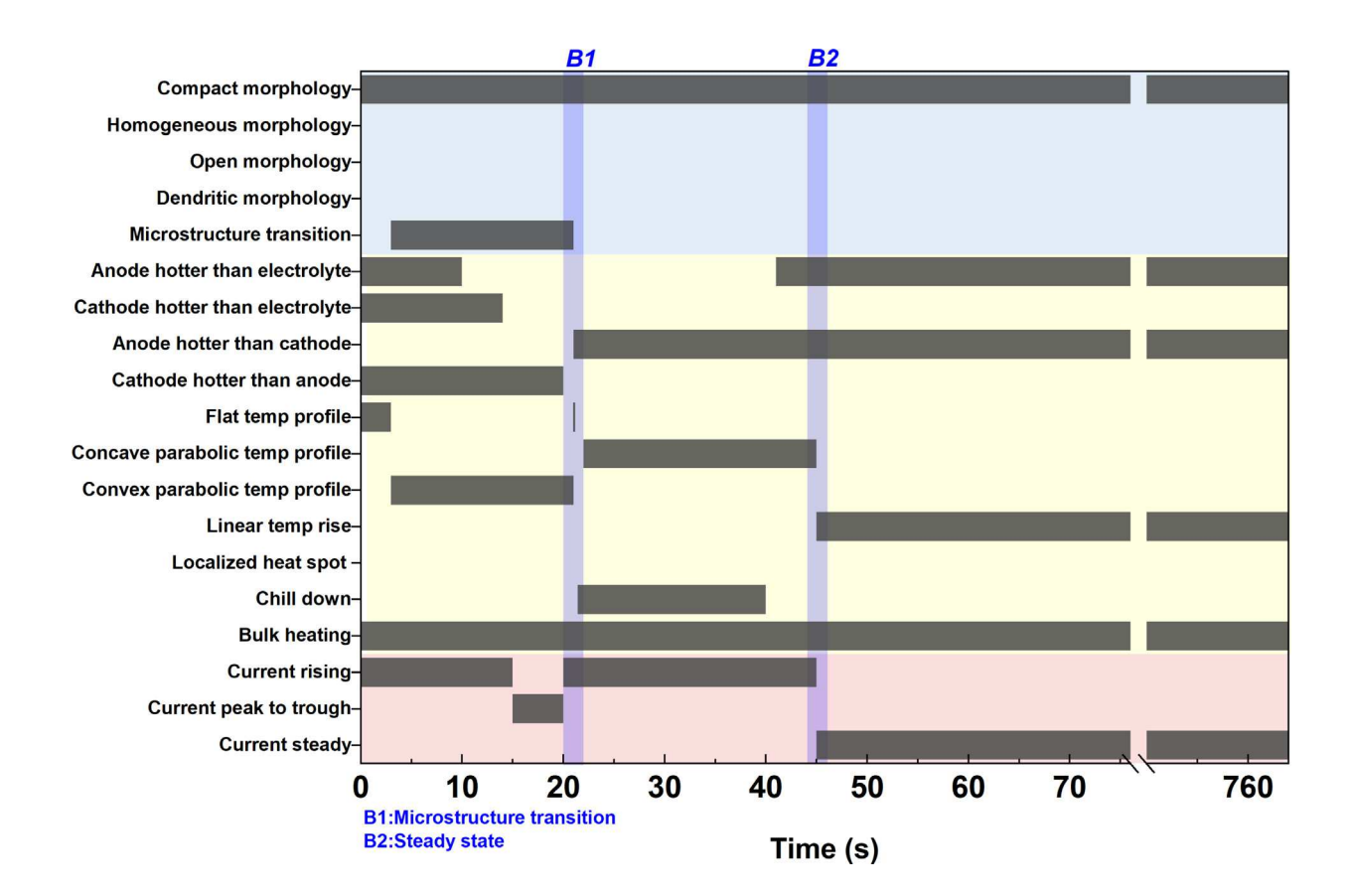


Fig. 10. Gantt chart for electrodeposition at 200 mM electrolyte concentration showing the correlation between the observed phenomena across three categories of observations: morphology (blue region), temperature (yellow region), and current changes (red region). Correlations of several phenomena are observed at B1 and B2 where the microstructural transition is completed and steady state current is reached, respectively.

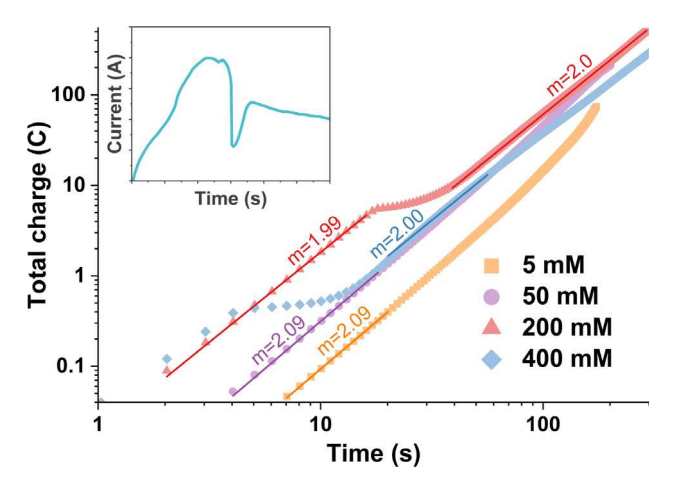


Fig. 11. Total charge vs. time plot at different electrolyte concentrations. The variable 'm' denotes the slope of the curves. Inset figure shows a typical current-time plot.

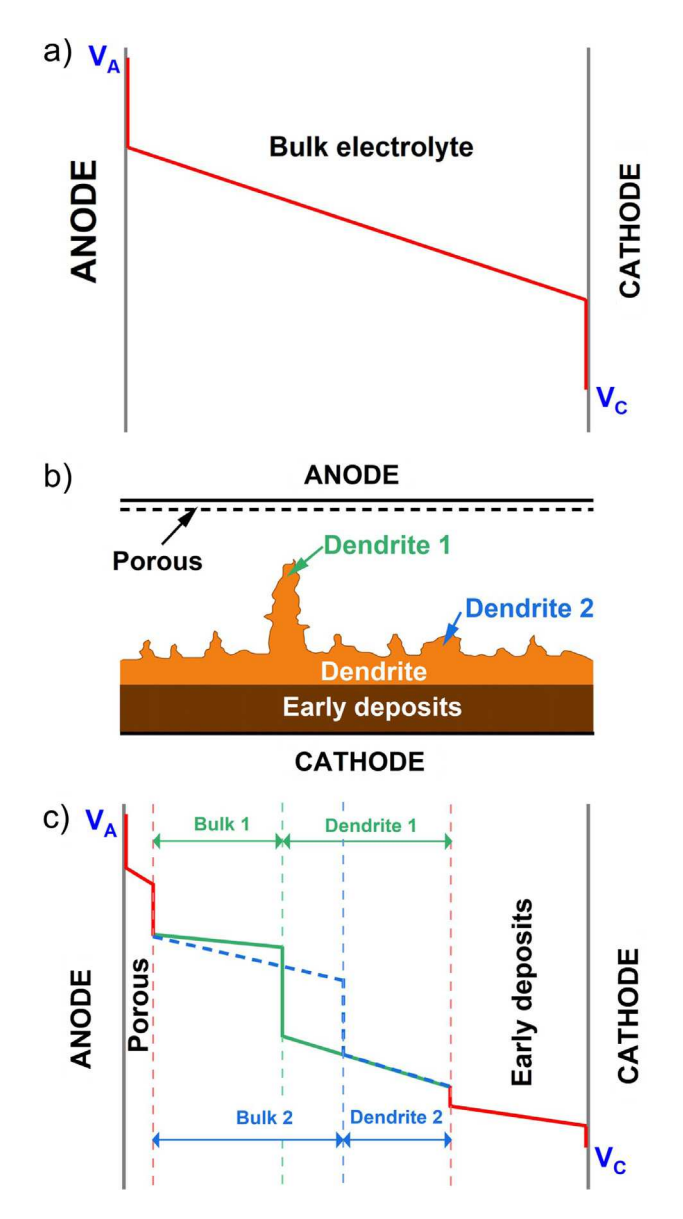


Fig. 12. (a) Initial electrochemical cell with linear potential drop across electrode. (b) Schematic of the electrochemical cell with different layers of deposited metal. (c) Electrochemical cell with multiple potential drops across the layers of deposited metal that decrease the potential drop across the bulk electrolyte solution.

electrochemical cell that stop electrodeposition. Fig. 12a shows that the initial electrochemical cell is simple with a potential drop across the solution. However, different layers start forming at the interface once dendrites start being deposited, as highlighted in Fig. 12b. As shown in Fig. 12c, the dendrite and porous layers cause additional potential drops in the cell. Assuming that the resistance in the dendrites is length dependent and a similar potential drop occurs across all solid–electrolyte interfaces, the bigger potential drop for dendrite 1 thereby decreases the potential drop across the solution (bulk regions 1 and 2). The potential drop across the solution is what drives mass transport of ions to the cathode to complete the reaction. If the resistance in the deposit, dendrite, and/or porous layer becomes too large, deposition will cease. The extent of the potential drop in these regions is dependent on the kinetics at the electrode.

These potential changes can explain why some dendrites cease to grow, as shown in Fig. 8, while other dendrites start to grow faster. Intuitively, one would expect that the fastest growing branch would have the highest potential drop across the solution (a larger driving force to grow) and would continue to grow and be the first to short the electrochemical cell. However, that is not what was observed here. Instead, the other deposits begin to grow. Interestingly, this new growth is darker in color, suggesting that it is composed of Cu<sub>2</sub>O. As discussed above, the deposition of Cu<sub>2</sub>O suggests that this region has a different localized pH. Given that this region of the electrode has become stagnant due to the enhanced growth front of the dendrites, the local pH can be different from the areas surrounding the fastest growing dendrite. Alternatively, the increased temperature that has built up in the electrochemical cell could require a larger  $\Delta pH$  to reach the Cu-Cu<sub>2</sub>O transition since the increase in local temperature (up to 7 to 8 °C) shifts the Pourbaix curve for the Cu<sub>2</sub>O to Cu transition to lower pH values (see Fig. S5 in the SI). Regardless, the local pH would be expected to become more acidic as this later stage growth continues. Indeed, the deposits at t = 175 s appear to be consistent with copper deposition that occurs at lower pH.

### 5. Conclusions

In this study, various morphologies were observed during electrodeposition from CuSO<sub>4</sub> at different concentrations using non-invasive in situ microscopy and thermometry. Depending on the initial electrolyte concentration, compact or dendritic growth morphologies were obtained. The specific morphology attained influences the dynamic behavior of the system. At high electrolyte concentrations, fast temperature rises occur but convection quickly dissipates the heat. The faster reactions generate large pH gradients that alter the chemistry of deposits and can even result in a receding growth front until all prior Cu<sub>2</sub>O has been converted to Cu. At low electrolyte concentrations, dendrites form early. The faster deposition rate at their tips likely leads to deposits with higher resistance. The higher resistance of the dendrites then becomes a source of localized heating. If the resistance becomes too high in a dendritic branch, then electrodeposition ceases to continue. The pH gradients are also slower to develop and, therefore, do not alter the chemistry of prior deposits. The study showed that many physicochemical, temperature, and current phenomena occurring during electrodeposition are correlated. Many of the changes were associated with the transformed microstructure and the establishment of steady-state current. Understanding the temporal evolution of temperature profiles and correlated changes to other parameters will be important to the performance and safety of electrochemical systems.

# CRediT authorship contribution statement

**Pinar Eribol:** Conceptualization, Methodology, Validation, Formal analysis, Investigation, Writing – review & editing, Visualization, Funding acquisition. **Sarathy K. Gopalakrishnan:** Conceptualization, Methodology, Software, Validation, Formal analysis, Investigation, Data curation, Writing – original draft, Writing – review & editing,

Visualization, Funding acquisition. **S.V. Diwakar:** Conceptualization, Software. **Abdelkrim Talbi:** Conceptualization. **Ranga Narayanan:** Conceptualization, Methodology, Resources, Writing – review & editing, Supervision, Funding acquisition. **Farzam Zoueshtiagh:** Conceptualization, Methodology, Resources, Data curation, Writing – review & editing, Supervision, Funding acquisition. **Kirk J. Ziegler:** Conceptualization, Methodology, Resources, Writing – review & editing, Visualization, Supervision, Funding acquisition.

### Declaration of competing interest

The authors declare the following financial interests/personal relationships which may be considered as potential competing interests: Kirk Ziegler and Ranga Narayanan report financial support was provided by National Science Foundation. Farzam Zoueshtiagh reports financial support was provided by French National Aerospace Research Centre.

### Data availability

Data will be made available on request.

### Acknowledgments

This work was partially supported by grants from the National Science Foundation, United States NSF-DMR-2004527, the University of Florida Space Research Initiative, United States, and the French Space Agency (CNES). PE acknowledges the financial support of The Scientific and Technological Research Council of Turkey (TUBITAK) 2219 - International Postdoctoral Research Fellowship. SKG acknowledges the travel support from Research Abroad for Doctoral Students (RAD) award, United States, Botic Family Scholars Professional Pathways Program award, France, Graduate Student Council travel award, United States, and University of Florida Office of Research travel fund, United States. RN acknowledges financial support from the William P. and Tracy Cirioli Professorship, United States. KJZ acknowledges financial support from the Dow Chemical Company Foundation Professorship, United States, the Charles A. Stokes Professorship, United States, and a Visiting Professorship from Université de Lille/IEMN, France.

# Appendix A. Supplementary data

Supplementary material related to this article can be found online at https://doi.org/10.1016/j.electacta.2023.142616. The Supporting Information is available free of charge at https://doi.org/10.1016/j.electacta.2023.142616.

Thermal data at 400 mM CuSO<sub>4</sub>, Gantt charts at 5, 50, and 400 mM CuSO<sub>4</sub>, effect of temperature on Pourbaix diagram, initial charge to cell at start of electrodeposition (PDF), Receding growth front video (MP4) and Fluorescent pH changes video (MP4).

### References

- [1] B.E. Conway, J.O. Bockris, The mechanism of electrolytic metal deposition, Proc. R. Soc. A 248 (1254) (1958) 394–403.
- [2] J. Bockris, M. Enyo, Mechanism of electrodeposition and dissolution processes of copper in aqueous solutions, Trans. Faraday Soc. 58 (1962) 1187–1202.
- [3] O. Brown, H. Thirsk, The rate-determining step in the electro-deposition of copper on copper from aqueous cupric sulphate solutions, Electrochim. Acta 10 (4) (1965) 383–393.
- [4] Y. Fukunaka, K. Okano, Y. Tomii, Z. Asaki, K. Kuribayashi, Electrodeposition of copper under microgravity conditions, J. Electrochem. Soc. 145 (6) (1998) 1876.
- [5] E. Mattsson, J. Bockris, Galvanostatic studies of the kinetics of deposition and dissolution in the copper+ copper sulphate system, Trans. Faraday Soc. 55 (1959) 1586–1601.
- [6] K. Popov, L.M. Djukić, M. Pavlović, M. Maksimović, The critical overpotential for copper dendrite formation, J. Appl. Electrochem. 9 (4) (1979) 527–531.

- [7] M.D. Pritzker, T.Z. Fahidy, Morphological stability of a planar metal electrode during potentiostatic electrodeposition and electrodissolution, Electrochim. Acta 37 (1) (1992) 103–112.
- [8] L. Hirt, S. Ihle, Z. Pan, L. Dorwling-Carter, A. Reiser, J.M. Wheeler, R. Spolenak, J. Vörös, T. Zambelli, Template-free 3D microprinting of metals using a forcecontrolled nanopipette for layer-by-layer electrodeposition, Adv. Mater. 28 (12) (2016) 2311–2315.
- [9] Z. Zong, H. Yu, L. Nui, M. Zhang, C. Wang, W. Li, Y. Men, B. Yao, G. Zou, Potential-induced copper periodic micro-/nanostructures by electrodeposition on silicon substrate, Nanotechnology 19 (31) (2008) 315302.
- [10] H. Kim, J.G. Kim, J.W. Park, C.N. Chu, Selective copper metallization of nonconductive materials using jet-circulating electrodeposition, Precis. Eng. 51 (2018) 153-159.
- [11] K. Wang, L. Niu, Z. Zong, M. Zhang, C. Wang, X. Shi, Y. Men, G. Zou, Direct electrodeposition of copper ladder structures on a silicon substrate, Cryst. Growth Des. 8 (2) (2008) 442–445.
- [12] B. Xu, J. Lee, D. Kwon, L. Kong, M. Pecht, Mitigation strategies for Li-ion battery thermal runaway: A review, Renew. Sustain. Energy Rev. 150 (2021) 111437.
- [13] M. Faraday, On a peculiar class of acoustical figures; and on certain forms assumed by groups of particles upon vibrating elastic surfaces, Philos. Trans. R. Soc. 121 (1831) 299–340.
- [14] J. Rayleigh, On the crispations of fluid resting upon a vibrating support, Lond. Edinb. Dublin Philos. Mag. J. Sci. 16 (97) (1883) 50–58.
- [15] J. Rayleigh, Investigation of the character of the equilibrium of an incompressible heavy fluid of variable density, Proc. Lond. Math. Soc. s1-14 (1) (1882) 170-177.
- [16] J. Melcher, G. Taylor, Electrohydrodynamics: A review of the role of interfacial shear stresses, Annu. Rev. Fluid Mech. 1 (1) (1969) 111–146.
- [17] S. Coriell, M. Cordes, W. Boettinger, R. Sekerka, Convective and interfacial instabilities during unidirectional solidification of a binary alloy, J. Cryst. Growth 49 (1) (1980) 13–28.
- [18] S.K. Gopalakrishnan, A. Ganesh, C.-C. Wang, M. Mango, K.J. Ziegler, R. Narayanan, Isolation of competing morphological patterns during microfluidic electrodeposition: Experimental confirmation of theory, Electrochim. Acta 398 (2021) 139205.
- [19] Q. BuAli, L. Johns, R. Narayanan, The growth of roughness during electrodeposition, Electrochim. Acta 51 (14) (2006) 2881–2889.
- [20] L.-G. Sundström, F.H. Bark, On morphological instability during electrodeposition with a stagnant binary electrolyte, Electrochim. Acta 40 (5) (1995) 599–614.
- [21] D.P. Barkey, R.H. Muller, C.W. Tobias, Roughness development in metal electrodeposition: I. Experimental results, J. Electrochem. Soc. 136 (8) (1989) 2199–2207.
- [22] D.P. Barkey, R.H. Muller, C.W. Tobias, Roughness development in metal electrodeposition: II. Stability theory, J. Electrochem. Soc. 136 (8) (1989) 2207–2214.
- [23] J.R. de Bruyn, Early stages of ramified growth in quasi-two-dimensional electrochemical deposition, Phys. Rev. E 53 (1996) R5561–R5564.
- [24] G.L.M.K.S. Kahanda, X.-q. Zou, R. Farrell, P.-z. Wong, Columnar growth and kinetic roughening in electrochemical deposition, Phys. Rev. Lett. 68 (1992) 3741–3744.
- [25] C. Léger, L. Servant, J.L. Bruneel, F. Argoul, Growth patterns in electrodeposition, Physica A 263 (1–4) (1999) 305–314.
- [26] F. Sagués, M.Q. López-Salvans, J. Claret, Growth and forms in quasi-twodimensional electrocrystallization, Phys. Rep. 337 (2000) 97–115.
- [27] A. Kuhn, F. Argoul, Spatiotemporal morphological transitions in thin-layer electrodeposition: The Hecker effect, Phys. Rev. E 49 (1994) 4298.
- [28] M. Schröter, K. Kassner, I. Rehberg, J. Claret, F. Sagués, Influence of ohmic heating on the flow field in thin-layer electrodeposition, Phys. Rev. E 66 (2002).
- [29] M.-Q. Lopez-Salvans, F. Sagués, J. Claret, J. Bassas, Further insights on dynamic morphological transitions in quasi-two-dimensional electrodeposition, Phys. Rev. E 56 (6) (1997) 6869.
- [30] A. Sukeri, M. Bertotti, Electrodeposited honeycomb-like dendritic porous gold surface: An efficient platform for enzyme-free hydrogen peroxide sensor at low overpotential, J. Electroanal. Chem. 805 (2017) 18–23.
- [31] K. Janzakova, M. Ghazal, A. Kumar, Y. Coffinier, S. Pecqueur, F. Alibart, Dendritic organic electrochemical transistors grown by electropolymerization for 3D neuromorphic engineering, Adv. Sci. 8 (2021) 2102973.
- [32] M. Datta, E. Lin, H.-W. Choi, M. McMaster, R. Brewer, D. Werner, J. Hom, G. Upadhya, S. Gopalakrishnan, F. Rebarber, Liquid cooling system for advanced microelectronics, ECS Trans. 6 (8) (2007) 13.
- [33] M. Datta, Microelectronic packaging trends and the role of nanotechnology, in: Electrochemical Nanotechnologies, Springer, 2010, pp. 227–253.
- [34] L. Huang, L. Liu, L. Lu, X. Feng, X. Han, W. Li, M. Zhang, D. Li, X. Liu, D.U. Sauer, M. Ouyang, A review of the internal short circuit mechanism in lithium-ion batteries: Inducement, detection and prevention, Int. J. Energy Res. 45 (11) (2021) 15707–15831
- [35] M.J. Loveridge, G. Remy, N. Kourra, R. Genieser, A. Barai, M.J. Lain, Y. Guo, M. Amor-Segan, M.A. Williams, T. Amietszajew, M. Ellis, R. Bhagat, D. Greenwood, Looking deeper into the Galaxy (Note 7), Batteries 4 (1) (2018) 3.

- [36] P. Grosfils, F. Dubois, C. Yourassowsky, A. De Wit, Hot spots revealed by simultaneous experimental measurement of the two-dimensional concentration and temperature fields of an exothermic chemical front during finger-pattern formation, Phys. Rev. E 79 (1) (2009) 017301.
- [37] D. Barkey, D. Watt, Z. Liu, S. Raber, The role of induced convection in branched electrodeposit morphology selection, J. Electrochem. Soc. 141 (5) (1994) 1206.
- [38] M. Schröter, K. Kassner, I. Rehberg, J. Claret, F. Sagués, Influence of ohmic heating on the flow field in thin-layer electrodeposition, Phys. Rev. E 66 (2) (2002) 026307.
- [39] P. Barvinschi, Numerical simulation of ohmic heating in idealized thin-layer electrodeposition cells, J. Optoelectron. Adv. Mater. 8 (1) (2006) 271.
- [40] K. Kim, S. Feng, Thermal mapping using infrared thermography, in: Application of Thermo-Fluidic Measurement Techniques, Elsevier, 2016, pp. 215–250.
- [41] I.P. Nagy, A. Keresztessy, J.A. Pojman, Periodic convection in the bromate-sulfite reaction: A "jumping" wave, J. Phys. Chem. 99 (15) (1995) 5385–5388.
- [42] M. Böckmann, B. Hess, S.C. Müller, Temperature gradients traveling with chemical waves, Phys. Rev. E 53 (5) (1996) 5498.
- [43] B. Majaron, W. Verkruysse, B.S. Tanenbaum, T.E. Milner, J.S. Nelson, Spectral variation of the infrared absorption coefficient in pulsed photothermal profiling of biological samples, Phys. Med. Biol. 47 (11) (2002) 1929.
- [44] M.Q. Brewster, Thermal Radiative Transfer and Properties, John Wiley & Sons, 1992.
- [45] C.A. Schneider, W.S. Rasband, K.W. Eliceiri, NIH Image to ImageJ: 25 years of image analysis, Nature Methods 9 (7) (2012) 671–675.
- [46] getSelectionCoordinates function, 2022, last accessed on 2022-11-04. URL https://imagej.nih.gov/ij/macros/SelectionCoordinates.txt.

- [47] J.R. Melrose, D.B. Hibbert, R.C. Ball, Interfacial velocity in electrochemical deposition and the hecker transition, Phys. Rev. Lett. 65 (1990) 3009.
- [48] M.Q. López-Salvans, F. Sagués, J. Claret, J. Bassas, Fingering instability in thin-layer electrodeposition: general trends and morphological transitions, J. Electroanal. Chem. 421 (1997) 205–212.
- [49] V. Fleury, M. Rosso, J.-N. Chazalviel, Geometrical aspect of electrodeposition: The Hecker effect, Phys. Rev. A 43 (1991) 6908–6916.
- [50] Z. Xu, K.M. Rosso, S. Bruemmer, Metal oxidation kinetics and the transition from thin to thick films, Phys. Chem. Chem. Phys. 14 (42) (2012) 14534–14539.
- [51] A. Seyeux, V. Maurice, P. Marcus, Oxide film growth kinetics on metals and alloys: I. Physical model, J. Electrochem. Soc. 160 (6) (2013) C189.
- [52] F. Morin, G. Beranger, P. Lacombe, Limits of application for Wagner's oxidation theory, Oxid. Met. 4 (1) (1972) 51–62.
- [53] S.B. Donald, J.A. Stanford, J.M. Haschke, D.D. Ashley, W.A. Talbot, D.J. Roberts, A.J. Nelson, B.W. Chung, W. McLean, Parabolic oxidation kinetics of a plutonium alloy at room temperature, Corros. Sci. 187 (2021) 109527.
- [54] M. Hakamada, T. Kuromura, Y. Chen, H. Kusuda, M. Mabuchi, Influence of porosity and pore size on electrical resistivity of porous aluminum produced by spacer method, Mater. Trans. 48 (1) (2007) 32–36.
- [55] F. Ternero, L.G. Rosa, P. Urban, J.M. Montes, F.G. Cuevas, Influence of the total porosity on the properties of sintered materials—A review, Metals 11 (5) (2021) 730.
- [56] N.S. Mbugua, M. Kang, Y. Zhang, N.J. Ndiithi, G. V. Bertrand, L. Yao, Electro-chemical deposition of Ni, NiCo alloy and NiCo-ceramic composite coatings—A critical review, Materials 13 (16) (2020) 3475.